Synthesis and thermoelectric properties of bismuth antimony telluride thermoelectric materials fabricated at various ball-milling speeds with yttria-stabilized zirconia ceramic vessel and balls

Mongkol Bumrungpon[a], Kenji Hirota[a], Katsuhiro Takagi[a], Kenichi Hanasaku[a], Toshiharu Hirai[a], Issei Morioka[a], Ryusuke Yasufuku[a], Masato Kitamura[a], and Kazuhiro Hasezaki[b]

[a]Graduate School of Advanced Technology and Science, Tokushima University, 2–1 Minamijyosanjima, Tokushima 770–8506, Japan

[b]Graduate School of Technology, Industrial, and Social Sciences, Tokushima University, 2–1 Minamijosanjima, Tokushima 770–8506, Japan

[*]Corresponding author: Kazuhiro Hasezaki

E-mail: hasezaki@tokushima-u.ac.jp

p-type $Bi_{0.3}Sb_{1.7}Te_{3.0}$ thermoelectric materials were fabricated at various ball-milling speeds with yttria-stabilized zirconia (YSZ) ceramic balls in an YSZ vessel, and then hot-pressed. The powders milled at speeds of or higher than 150 rpm were completely alloyed and single-phase $Bi_{0.3}Sb_{1.7}Te_{3.0}$ was obtained. The grain size of a disk sintered at 350 °C was approximately 1 μm at a fracture surface. The Seebeck coefficients of sintered disks fabricated by YSZ milling were higher while their electrical conductivities were lower than those of disks fabricated by using a stainless-steel vessel and Si_3N_4 balls, as the YSZ milling suppressed the contamination by materials acting as carrier dopants in the $Bi_{0.3}Sb_{1.7}Te_{3.0}$ bulk. The contamination from the YSZ vessel and milling balls did not affect the phonon thermal conductivities of the $Bi_{0.3}Sb_{1.7}Te_{3.0}$ bulk materials. The dimensionless figure of merit *ZT* of the sample milled at 150 rpm with

the YSZ vessel and balls and sintered at 350 °C was approximately 1.7 times that of the sample milled with the stainless-steel vessel and Si_3N_4 balls. *ZT* remained above 1.0 and reached the peak of 1.16 (α: 295 μV/K, σ: 4.16 ×10^4 S/m, κ: 0.94 W/(m K)) at room temperature for the sample milled at 130 rpm and hot-pressed at 350 °C. Thus, the thermoelectric properties can be improved by selecting appropriate milling vessels and balls.

Keywords: Milling, Hot pressing, Electrical properties, ZrO_2

1. Introduction

Thermoelectric materials through which heat is directly converted to electricity can enable the use of unutilized energy, which can reduce the CO_2 emission [1]. In addition, the thermoelectricity can be used in energy-harvesting power generation and wearable devices [2,3]. In recent years, various thermoelectric materials have been investigated including skutterudite [4–7], antimonides [8–11], and cuprous chalcogenide [12–14].

The efficiency of a thermoelectric material is defined by its dimensionless figure of merit ZT:

$$ZT = \alpha^2\sigma T/\kappa = \alpha^2\sigma T/(\kappa_{\mathrm{phonon}} + \kappa_{\mathrm{carrier}}) = \alpha^2\sigma T/(\kappa_{\mathrm{phonon}} + L\sigma T), \quad (1)$$

where α, σ, κ, T, κ_{phonon}, $\kappa_{\mathrm{carrier}}$, and L are the Seebeck coefficient (V/K), electrical conductivity (S/m), thermal conductivity (W/(m K)), absolute temperature (K), phonon thermal conductivity (W/(m K)), carrier thermal conductivity (W/(m K)), and Lorenz number, respectively. The thermal conductivity κ of a thermoelectric material is generally the sum of the phonon and carrier components [15]. The Lorenz number of a metal, 2.45×10^{-8} W/(S K^2), is obtained by using the Wiedemann–Franz law [16]. Bi_2Te_3-based materials exhibit high ZT values, approximately 1.0 near room temperature, and are promising for use in energy-harvesting power generation and wearable thermoelectric devices [17,18]. Bi_2Te_3-based materials belong to the *R3m* space group and exhibit rhombohedral crystal structures as well as anisotropic physical and thermoelectric properties [19]. Extensive studies have focused on the development of fabrication methods to improve the ZT values of Bi_2Te_3-based materials [20–22]. Two main strategies are used. One of them involves hot extrusion [23,24] and high-pressure torsion [25] because anisotropic thermoelectric properties can be obtained by plastic deformation under anisotropic fabrication conditions. The other strategy involves dopant addition [26–29], nanomaterial dispersion [30–34], and mechanical alloying

(MA) [35,36] by powder metallurgy [37,38] under isotropic fabrication conditions.

When powder metallurgy methods are used for the fabrication of Bi_2Te_3-based materials, the properties of the end product powder depend on the milling energy and composition, size, and size distribution of the milling balls [39]. Higher temperatures and milling energy tend to yield large powder grains [40]. However, the relationships between the milling energy, sintering conditions, and thermoelectric properties of bulk materials have not been clearly understood. The milling energy depends on the rotational speed and ball-milling apparatus. A *p*-type $Bi_{0.3}Sb_{1.7}Te_{3.0}$ thermoelectric semiconductor with a dimensionless figure of merit $ZT = 1.01$ was fabricated by milling with Si_3N_4 balls in a stainless-steel vessel at various high rotational speeds and hot pressing (HP). However, the thermoelectric properties were weakened by the planetary-ball-milling rotational speed because of metal contamination with iron and chromium from the milling vessels [41]. If vessels and milling balls consisting of appropriate materials are selected to avoid reactions with the milled powder, high *ZT* values can be obtained. Yttria-stabilized zirconia (YSZ) ceramics are suitable materials for the milling vessel and balls with high fracture toughnesses [42].

In this study, *p*-type $Bi_{0.3}Sb_{1.7}Te_{3.0}$ thermoelectric materials were fabricated by a MA–HP process with YSZ milling vessel and balls, which did not react with the milled powder. The relationships between the milling energy, sintering conditions, and thermoelectric properties of the resulting samples were investigated.

2. Materials and Methods

The milled powder was stoichiometric ($Bi_{0.3}Sb_{1.7}Te_{3.0}$); no dopants were added [43]. The constituent elements, high-purity Bi (99.999%), Sb (99.9999%), and Te (99.9999%), with grain sizes of several millimeters (Kojundo Chemical Laboratory Co.,

Ltd., Saitama, Japan) weighed according to $Bi_{0.3}Sb_{1.7}Te_{3.0}$. The raw grains were placed in the YSZ vessel with milling balls in an argon-filled glove box. The YSZ vessel (capacity: 0.25 L) was sealed inside the box to reduce exposure to air. The YSZ milling balls were 25 mm in diameter. The YSZ vessel and milling balls were used to avoid reactions with the milled powder. The milling provides partial-to-complete alloying, depending on the milling rotational speed and milling vessel and ball materials. The effects of the milling rotational speed on the degree of alloying in the milling with the YSZ vessel and balls were investigated. The weight ratio of milling balls to raw materials, apparatus, and handling procedures were the same as those used previously with a stainless-steel vessel and Si_3N_4 balls [41]. The weight ratio of YSZ milling balls to raw materials was 20:1. The milling was performed in a Fritsch P-5 planetary ball mill for 30 h. The rotational speed of the main disk mounted on the milling vessel was 110–180 rpm. The milling vessel was rotated around its axis. The ratio of the rotational speed of the planetary disk to that of the milling vessel was fixed at 1:-2.18. The resulting milled powder was completely passed through a polymer mesh sieve (diameter: 150 μm); no elemental grains or other components remained on the sieve mesh surface in each fabrication. The sieved milled powders were analyzed by X-ray diffraction (XRD; Rigaku Multiflex diffractometer) to confirm the alloying of the milled powder and to determine whether contamination by the attrition of the milling balls and vessel occurred. The XRD patterns were recorded with Cu K_α radiation at a step size of 0.1° and step speed of 1.0 s/step in the Bragg angle range 2θ of 20–90°. The completely alloyed milled powder obtained at the minimum rotational speed was used to investigate the effects of the HP temperature and milling vessel and ball materials. The thermoelectric properties were expected to depend on the sintering temperature and milling vessel and ball materials.

The sieved milled powder was set in a HP mold in an argon-filled glove box. The HP mold filled with the milled powder was exposed only to air during the transportation between the argon-filled glove box and HP chamber. After the powder-filled HP mold was placed in the HP chamber, the HP chamber was evacuated to below 0.4 Pa. The milled powder was sintered under an axial pressure of 147 MPa in an argon atmosphere.

The sintered and YSZ-milled $Bi_{0.3}Sb_{1.7}Te_{3.0}$ bulk materials were investigated to determine the relationships between the structure, metallography, and thermoelectric properties and sintering temperature at the minimum rotational speed needed to achieve the complete alloying of the milled powder. The sintering temperature providing the best thermoelectric properties was determined. The powder milled at the minimum rotational speed providing the complete alloying was sintered at 100–400 °C under an axial compressive pressure of 147 MPa by HP in an argon atmosphere. The sintered compact was a cylinder having a height of 9 mm and diameter of 10 mm. The sintered compact was cut into disks having thicknesses of 1.0 mm and diameters of 10 mm. The disks obtained from the cylinder ends were not used in the experiments because they were affected by the plastic deformation and exhibited anisotropic thermoelectric properties owing to the HP [44,45]. Only disks obtained from the center of the cylinder were used in to investigate microstructures, densities, and thermoelectric properties. These disks were investigated by XRD and metallographic observations; their relative densities, Seebeck coefficients, and electrical and thermal conductivities were determined.

The XRD patterns in all out-of-plane directions of the disks were recorded with Cu K_α radiation at a step size of 0.1° and step speed of 5.0 s/step in the Bragg angle range 2θ of 10–110° (Rigaku SmartLab).

The microstructures and elemental distribution profiles in the out-of-plane directions

of the disks sintered at 100 °C and 350 °C were analyzed by scanning electron microscopy (SEM; JEOL, JSM-6510A) and energy-dispersive X-ray spectroscopy (EDS) in the same areas. The densities of the disks sintered at 100 °C and 350 °C were measured by using the Archimedes' method at room temperature.

The Seebeck coefficients α were determined at room temperature by using the thermal contact method [46]. The results were confirmed by using a standard Seebeck-coefficient material (SRM 3451) [47]. The accuracy of the Seebeck coefficients was within ±2%. The electrical conductivities σ were measured at room temperature by using the four-point probe method and constructed 2182A/6220 (Keithley Instruments, Inc.) delta-mode electrical resistance system. The probe material and spacing were tungsten carbide and 1.00 mm, respectively. The electrical conductivity measurements were confirmed by the ohmic contact [48]. The accuracy of the electrical conductivity was within ±1%. The thermal conductivities κ were measured at room temperature under a 1 Pa vacuum by using the static comparison method [49,50]. A quartz disk with a thickness of 1.0 mm and diameter of 10 mm was used as a reference material (κ = 1.411 W/(m K)). The accuracy of the thermal conductivity measurements was confirmed to be within ±1% by using the same quartz disk for both measurement and reference positions [48]. The phonon and carrier thermal conductivities were calculated by using Equation (1).

The dimensionless figures of merit *ZT* of the thermoelectric materials at room temperature were estimated by using Equation (1).

The thermoelectric properties were expected to change with the milling rotational speed and milling vessel and ball materials. The effects on the thermoelectric properties of the sintered $Bi_{0.3}Sb_{1.7}Te_{3.0}$ bulk materials fabricated by YSZ milling and sintered at the optimal temperature were investigated to obtain the maximum *ZT*. The powders

milled at 110–180 rpm, sintered at the optimal temperature, and subjected to HP under an axial compressive pressure of 147 MPa in an argon atmosphere exhibited the maximum *ZT*. The effects of the rotational speed on the thermoelectric properties of the sintered $Bi_{0.3}Sb_{1.7}Te_{3.0}$ fabricated by milling with the YSZ vessel and balls were investigated at the optimal sintering temperature to obtain the maximum *ZT*.

3. Results and Discussion

3.1 Dependence of the complete alloying of the $Bi_{0.3}Sb_{1.7}Te_{3.0}$ powder by YSZ milling on the milling rotational speed

All milled $Bi_{0.3}Sb_{1.7}Te_{3.0}$ powders were passed through a sieve with a diameter of 150 μm; no materials remained on the polymer sieve mesh surface. Fig. 1 shows the XRD patterns of the milled $Bi_{0.3}Sb_{1.7}Te_{3.0}$ powders, with diffraction peaks originating from only Bi, Sb, Te, and $Bi_{0.3}Sb_{1.7}Te_{3.0}$ [29]. The standard peaks of $Bi_{0.3}Sb_{1.7}Te_{3.0}$ (Inorganic Crystal Structure Database (ICSD) #184248) are indicated by vertical lines for comparison. Notably, no peaks originated from the milling vessel and balls or other materials were observed. The powders milled at rotational speeds of or higher than 150 rpm were completely alloyed; a single phase of $Bi_{0.3}Sb_{1.7}Te_{3.0}$ was obtained. The threshold milling speed for the complete alloying with the YSZ vessel and balls is equal to that for a stainless-steel vessel and Si_3N_4 balls [41]. The threshold milling speed for MA depends on the milling energy, not on the milling vessel and ball materials and particle size, because the milling kinetic energy is proportional to the milling mass ratio and velocity. The milling mass ratio and velocity for the YSZ vessel and balls were the same as those for a stainless-steel vessel and Si_3N_4 balls [40].

The milling at 150 rpm provided a single-phase $Bi_{0.3}Sb_{1.7}Te_{3.0}$ powder, which was used

to clarify the effects of the HP temperature and milling vessel and ball materials on the homogeneously synthesized materials.

3.2 $Bi_{0.3}Sb_{1.7}Te_{3.0}$ powder sintered at the optimal temperature and milled at the minimum rotational speed needed for complete alloying

All sintered samples were *p*-type semiconductors. Fig. 2 shows the XRD patterns of the $Bi_{0.3}Sb_{1.7}Te_{3.0}$ disks sintered at 100–400 °C and milled at 150 rpm; main *hkl* indices of $Bi_{0.3}Sb_{1.7}Te_{3.0}$ are also shown [29]. The standard peaks of $Bi_{0.3}Sb_{1.7}Te_{3.0}$ (ICSD #184248) are indicated by vertical lines for comparison. Notably, no peaks originated from materials other than $Bi_{0.3}Sb_{1.7}Te_{3.0}$, e.g., from the YSZ milling vessel and balls, were observed. The patterns show that all sintered disks were single-phase $Bi_{0.3}Sb_{1.7}Te_{3.0}$.

Fig. 3(a) shows an SEM image of the $Bi_{0.3}Sb_{1.7}Te_{3.0}$ disk sintered at 100 °C and milled at 150 rpm. Fig. 3(b), (c), and (d) show the elemental distributions of Bi, Sb, and Te, respectively, determined by EDS. Large numbers of pores and voids are observed in Fig. 3(a). Fig. 3(b)–(d) show that Bi, Sb, and Te were homogeneously dispersed in the $Bi_{0.3}Sb_{1.7}Te_{3.0}$ disk.

Fig. 4(a) and (b) show SEM images of a cross section and fracture surface, respectively, of a $Bi_{0.3}Sb_{1.7}Te_{3.0}$ disk sintered at 350 °C and milled at 150 rpm. The $Bi_{0.3}Sb_{1.7}Te_{3.0}$ disk had dense and fine grains. The grain size was approximately 1 μm at the fracture surface, similar to that for ball milling with a stainless-steel vessel and Si_3N_4 balls [27]. These results show that the contamination by the attrition of the milling vessel and balls and rotational speed did not affect the matrix grain growth [41].

Fig. 5(a) shows an SEM image of the $Bi_{0.3}Sb_{1.7}Te_{3.0}$ disk sintered at 350 °C and milled at 150 rpm. Fig. 5(b)–(f) show the elemental distributions of Bi, Sb, Te, Zr, and Y,

respectively, determined by EDS. Fig. 5(a) shows that the degree of sintering was higher than that in Fig. 3(a). A structured dense material similar to that in Fig. 4 was obtained. Particles with sizes of several micrometers were observed in the matrix. Fig. 5(e) and (f) indicate that these particles correspond to YSZ. YSZ did not react with $Bi_{0.3}Sb_{1.7}Te_{3.0}$ because a reaction layer between YSZ and $Bi_{0.3}Sb_{1.7}Te_{3.0}$ matrix was not observed.

The relative densities of the $Bi_{0.3}Sb_{1.7}Te_{3.0}$ disks sintered at 100 °C and 350 °C and milled at 150 rpm were 95.5% and 99.2%, respectively, calculated based on an absolute density of 6.73 g/cm^3 [29]. The relative density increased with the sintering temperature. The increase in relative density with the sintering temperature is in agreement with the SEM images in Figs. 3(a) and 4(a).

Fig. 6 shows the relationship between the electrical conductivity and sintering temperature for the $Bi_{0.3}Sb_{1.7}Te_{3.0}$ disks milled at 150 rpm at room temperature. The open circle corresponds to a $Bi_{0.3}Sb_{1.7}Te_{3.0}$ disk sintered at 350 °C and milled at 150 rpm with a stainless-steel vessel and Si_3N_4 balls [41]. The electrical conductivity of the $Bi_{0.3}Sb_{1.7}Te_{3.0}$ disk milled at 150 rpm with the YSZ milling vessel and balls increased with the sintering temperature and reached the maximum at 350 °C because the sintering of $Bi_{0.3}Sb_{1.7}Te_{3.0}$ was complete, as shown in Figs. 3(a) and 4(a). The electrical conductivities of the disks obtained by milling with the YSZ vessel and balls were considerably lower than those obtained by milling with the stainless-steel vessel and Si_3N_4 balls. The metal contaminants form the stainless-steel vessel acted as carrier dopants, which affected the electrical conductivity. However, Fig. 5(a) shows YSZ particles with sizes of several micrometers in the matrix; the contamination by the YSZ vessel and balls was not detrimental to the electrical conductivity.

Fig. 7 shows the relationship between the Seebeck coefficient and sintering temperature for the $Bi_{0.3}Sb_{1.7}Te_{3.0}$ disks milled at 150 rpm at room temperature. The

open circle corresponds to the $Bi_{0.3}Sb_{1.7}Te_{3.0}$ disk sintered at 350 °C and milled at 150 rpm with the stainless-steel vessel and Si_3N_4 balls [41]. The Seebeck coefficient of the sintered $Bi_{0.3}Sb_{1.7}Te_{3.0}$ disk milled at 150 rpm with the YSZ vessel and balls increased with the sintering temperature and reached the maximum at 250 °C because the sintering of $Bi_{0.3}Sb_{1.7}Te_{3.0}$ was complete, as shown in Figs. 3(a) and 4(a). The Seebeck coefficients of the samples obtained by milling with the YSZ vessel and balls were considerably higher than that of the sample milled with the stainless-steel vessel and Si_3N_4 balls. The milling in the stainless-steel vessel decreased the Seebeck coefficient, which could be explained through the same considerations as those for the effect on the electrical conductivity, i.e., the contaminants from the stainless-steel vessel acted as carrier dopants. In contrast, in the case of milling with the YSZ vessel and balls, the Seebeck coefficients remained high and were not detrimentally affected by contaminants. The inverse relationship between the Seebeck coefficient and electrical conductivity is consistent with the dependences of the Seebeck coefficient and electrical conductivity on the concentration of free carriers [1,15]. High Seebeck coefficients and low electrical conductivities were achieved by the YSZ milling, which shows that the contamination was suppressed. Therefore, no contaminants acted as carrier dopants in the $Bi_{0.3}Sb_{1.7}Te_{3.0}$ thermoelectric materials.

Fig. 8 shows the relationships between the total, phonon, and carrier thermal conductivities and sintering temperature for the $Bi_{0.3}Sb_{1.7}Te_{3.0}$ disks milled at 150 rpm. The open symbols correspond to the $Bi_{0.3}Sb_{1.7}Te_{3.0}$ disk sintered at 350 °C and milled at 150 rpm with the stainless-steel vessel and Si_3N_4 balls [41]. The phonon and carrier thermal conductivities were estimated by using equation (1). The thermal conductivity of the sintered $Bi_{0.3}Sb_{1.7}Te_{3.0}$ disk milled at 150 rpm with the YSZ vessel and balls increased with the sintering temperature and reached the maximum at 350 °C because

the sintering of $Bi_{0.3}Sb_{1.7}Te_{3.0}$ was complete. The total thermal conductivity of the disk sintered at 350 °C and milled with the YSZ vessel and balls was lower than that of the sample obtained by milling with the stainless-steel vessel and Si_3N_4 balls, because of the difference between the carrier thermal conductivities. The carrier thermal conductivities of the samples milled with the YSZ vessel and balls were lower than that of the sample milled with the stainless-steel vessel and Si_3N_4 balls. The contaminants from the stainless-steel vessel acted as carrier dopants, which affected the carrier thermal conductivity. In contrast, the phonon thermal conductivities were similar to each other and were not affected by the milling vessel and ball materials; no contaminants from the milling vessel and balls affected the phonon thermal conductivity. This is consistent with the matrix grain growth unaffected by the milling media, as shown in Fig. 4.

Fig. 9 shows the relationship between the dimensionless figure of merit *ZT* and sintering temperature for the $Bi_{0.3}Sb_{1.7}Te_{3.0}$ disks milled at 150 rpm at room temperature. The open circle corresponds to the $Bi_{0.3}Sb_{1.7}Te_{3.0}$ disk sintered at 350 °C and milled at 150 rpm with the stainless-steel vessel and Si_3N_4 balls [41]. The maximum *ZT*, 1.14 (α = 292 μV/K, σ = 4.41 × 10^4 S/m, κ = 0.99 W/(m K)) at room temperature, was achieved for the disk sintered at 350 °C. *ZT* of the sample fabricated by milling at 150 rpm with the YSZ vessel and balls and sintered at 350 °C was approximately 1.7 times that of the sample fabricated by milling with the stainless-steel vessel and Si_3N_4 balls. However, Fig. 5 shows YSZ particles with sizes of several micrometers in the matrix. This indicates that the contaminants from the YSZ vessel and balls improved the dimensionless figure of merit *ZT*, as the YSZ milling did not produce contaminants acting as carrier dopants for the $Bi_{0.3}Sb_{1.7}Te_{3.0}$ thermoelectric material.

These results show that the milling with YSZ improved the dimensionless figure of

merit of $Bi_{0.3}Sb_{1.7}Tae_{3.0}$. The investigation of the thermoelectric properties of the sintered $Bi_{0.3}Sb_{1.7}Te_{3.0}$ bulk materials fabricated by YSZ milling showed that the milling at a fixed rotational speed and sintering at 350 °C provided the maximum *ZT*.

3.3 Optimal milling speed to achieve the maximum *ZT* of the $Bi_{0.3}Sb_{1.7}Te_{3.0}$ disk sintered at the optimal temperature

All sintered samples were *p*-type semiconductors. Fig. 10 shows the XRD patterns of the disks fabricated by milling at 110–180 rpm and sintered at 350 °C; main *hkl* indices of $Bi_{0.3}Sb_{1.7}Te_{3.0}$ are shown [29]. Only peaks originated from $Bi_{0.3}Sb_{1.7}Te_{3.0}$ were observed; no peaks originated from the YSZ vessel and balls were observed. All sintered disks were identified as single-phase $Bi_{0.3}Sb_{1.7}Te_{3.0}$. The remaining unalloyed materials when the milling was performed at or below 130 rpm (Fig. 1) disappeared and $Bi_{0.3}Sb_{1.7}Te_{3.0}$ was formed during the subsequent sintering. All milled powders were completely alloyed by the HP [41]. The XRD patterns show that the contaminants from the milling vessel and balls did not affect the alloying during the subsequent sintering.

Fig. 11 shows the relationship between the electrical conductivity and milling speed for the $Bi_{0.3}Sb_{1.7}Te_{3.0}$ disks sintered at 350 °C and milled with the YSZ vessel and balls at room temperature. The solid line shows the data for the $Bi_{0.3}Sb_{1.7}Te_{3.0}$ disks sintered at 350 °C and milled with the stainless-steel vessel and Si_3N_4 balls [41]. The electrical conductivity of the $Bi_{0.3}Sb_{1.7}Te_{3.0}$ disk sintered at 350 °C and milled with the YSZ vessel and balls was constant up to 150 rpm and increased at 180 rpm. The differences between the electrical conductivities of the samples fabricated by milling with the YSZ vessel and balls and those of the samples milled with the stainless-steel vessel and Si_3N_4 balls increased with the milling speed. The amounts of contaminants from the

milling vessel and balls increased with the milling speed because of the increased milling energy. The effect of the stainless-steel vessel on the electrical conductivity was larger than the effect of the YSZ vessel because the contaminants from the stainless-vessel acted as carrier dopants. In contrast, the YSZ milling suppressed the contamination by materials acting as carrier dopants for the $Bi_{0.3}Sb_{1.7}Te_{3.0}$ thermoelectric material. The electrical conductivity of the $Bi_{0.3}Sb_{1.7}Te_{3.0}$ disk milled with the YSZ vessel and balls was constant up to 150 rpm, but was slightly increased at 180 rpm. The input milling energy was converted to thermal energy. The milling vessel interior was heated by the high-energy milling. The heat inside the vessel was released to the outside through conduction by the vessel material. The thermal conductivities of YSZ and stainless steel are approximately 3 and 16 W/(m K), respectively [51,52]. Therefore, the heat in the YSZ vessel might be more insulated than that in the stainless-steel vessel. The process temperature in the YSZ milling was higher than that in the milling with the stainless-steel vessel and Si_3N_4 balls. Furthermore, the equilibrium vapor pressures of Bi, Sb, and Te are approximately 1×10^{-5}, 1×10^{-4}, and 0.3 Pa, respectively, at 350 °C [53,54]. Therefore, evacuation of Te would occur, which would lead to Te deficiency in $Bi_{0.3}Sb_{1.7}Te_{3.0}$ during the milling at 180 rpm. The Te deficiency created during the high-energy YSZ milling leads to an increase in electrical conductivity and decrease in Seebeck coefficient of $Bi_{0.3}Sb_{1.7}Te_{3.0+x}$ [27].

Fig. 12 shows the relationship between the Seebeck coefficient and milling speed for the $Bi_{0.3}Sb_{1.7}Te_{3.0}$ disks sintered at 350 °C and milled with the YSZ vessel and balls at room temperature. The solid line shows the data for the $Bi_{0.3}Sb_{1.7}Te_{3.0}$ disks sintered at 350 °C and milled with the stainless-steel vessel and Si_3N_4 balls [41]. The Seebeck coefficient of the $Bi_{0.3}Sb_{1.7}Te_{3.0}$ disk sintered at 350 °C and milled with the YSZ vessel

and balls was constant up to 150 rpm and slightly decreased at 180 rpm. The differences between the Seebeck coefficients of the samples milled with the YSZ vessel and balls and those of the samples milled with the stainless-steel vessel and Si_3N_4 balls increased up to 150 rpm. The contamination by the milling vessel increased with the milling speed because of the increased milling energy. However, the YSZ milling suppressed the contamination by materials acting as carrier dopants for $Bi_{0.3}Sb_{1.7}Te_{3.0}$. The Seebeck coefficient of the $Bi_{0.3}Sb_{1.7}Te_{3.0}$ disk milled with the YSZ vessel and balls was slightly decreased at 180 rpm, which could be explained through the same considerations as those for the effect on the electrical conductivity, i.e., the Te evacuation during the milling led to the Te deficiency in $Bi_{0.3}Sb_{1.7}Te_{3.0}$ milled at 180 rpm. The Te deficiency created during the high-energy YSZ milling led to a decrease in Seebeck coefficient of $Bi_{0.3}Sb_{1.7}Te_{3.0+x}$, which is consistent with the dependences of the Seebeck coefficient and electrical conductivity on the concentration of free carriers [1,15,27].

These results show that the YSZ milling suppressed the introduction of contaminants acting as carrier dopants for $Bi_{0.3}Sb_{1.7}Te_{3.0.}$ Furthermore, the Te evacuation during the high-energy YSZ milling, e.g., at 180 rpm, led to the Te deficiency in $Bi_{0.3}Sb_{1.7}Te_{3.0}$.

Fig. 13 shows the relationships between the total, phonon, and carrier thermal conductivities and milling speed for the $Bi_{0.3}Sb_{1.7}Te_{3.0}$ disks sintered at 350 °C and milled with the YSZ vessel and balls at room temperature. The total, phonon, and carrier thermal conductivities of the $Bi_{0.3}Sb_{1.7}Te_{3.0}$ disks sintered at 350 °C and milled with the stainless-steel vessel and Si_3N_4 balls are also shown [41]. The phonon and carrier thermal conductivities were estimated by using equation (1). The differences between the total thermal conductivities of the samples sintered and milled with the YSZ vessel and balls and those of the samples milled with the stainless-steel vessel

and Si_3N_4 balls increased because of the differences between their carrier thermal conductivities. The carrier thermal conductivity of the $Bi_{0.3}Sb_{1.7}Te_{3.0}$ disk sintered at 350 °C and milled with the YSZ vessel and balls was constant up to 150 rpm and slightly increased at 180 rpm. This is consistent with the effects of the milling on the Seebeck coefficients and electrical conductivities by the suppression of contaminants acting as carrier dopants and creation of Te deficiency [27]. The phonon thermal conductivities of the sintered $Bi_{0.3}Sb_{1.7}Te_{3.0}$ disks milled with the YSZ vessel and balls were constant and similar to those of the samples milled with the stainless-steel vessel and Si_3N_4 balls. The contaminants from the YSZ vessel and balls did not affect the phonon thermal conductivity. This is consistent with the results in Fig. 4, which show that the milling vessel and balls did not affect the matrix grain growth.

Fig. 14 shows the relationship between the dimensionless figure of merit *ZT* and milling speed for the $Bi_{0.3}Sb_{1.7}Te_{3.0}$ disks sintered at 350 °C. The solid line shows the data for the $Bi_{0.3}Sb_{1.7}Te_{3.0}$ disks sintered at 350 °C and milled with the stainless-steel vessel and Si_3N_4 balls [41]. The *ZT* values of the samples milled with the YSZ vessel and balls were constant, unlike those of the samples milled with the stainless-steel vessel and Si_3N_4 balls. The contaminants from the YSZ vessel and milling balls improved *ZT*. *ZT* remained above 1.0 and reached the peak of 1.16 (α = 295 μV/K, σ = 4.16×10^4 S/m, κ = 0.94 W/(m K)) at room temperature at 130 rpm.

These results indicate that the milling with the YSZ vessel and balls improved the dimensionless figure of merit because it suppressed the contamination by materials acting as carrier dopants for the $Bi_{0.3}Sb_{1.7}Te_{3.0}$ thermoelectric material. These results show that the improvements in thermoelectric properties were largely affected by the milling vessel and ball materials.

4. Conclusions

In this study, *p*-type $Bi_{0.3}Sb_{1.7}Te_{3.0}$ thermoelectric materials were fabricated by the MA–HP process at various milling speeds with the YSZ vessel and balls. The thermoelectric properties of the resulting samples were investigated. The results can be summarized as follows.

(1) The powders milled at rotational speeds of or higher than 150 rpm were completely alloyed and single-phase $Bi_{0.3}Sb_{1.7}Te_{3.0}$ was obtained. The threshold milling speed for complete alloying by milling with the YSZ vessel and balls was equal to that for the milling with the stainless-steel vessel and Si_3N_4 balls.

(2) The grain size of the disk sintered at 350 °C was approximately 1 μm at the fracture surface. The attrition of the milling vessel and balls was not detrimental to the matrix grain growth at given milling ball-to-material weight ratio and milling speed.

(3) The disks milled with the YSZ vessel and balls exhibited higher Seebeck coefficients α and lower electrical conductivities σ than those of the disks milled with the stainless-steel vessel and Si_3N_4 balls. The YSZ milling suppressed the contamination by materials acting as carrier dopants for $Bi_{0.3}Sb_{1.7}Te_{3.0}$. The contaminants from the YSZ vessel and balls did not affect the phonon thermal conductivity.

(4) *ZT* of the sample milled at 150 rpm with the YSZ vessel and balls and sintered at 350 °C was approximately 1.7 times that of the sample milled with the stainless-steel vessel and Si_3N_4 balls.

(5) *ZT* remained above 1.0 and reached the peak of 1.16 (α = 295 μV/K, σ = 4.16 × 10^4 S/m, κ = 0.94 W/(m K)) at room temperature for the sample milled at

130 rpm and hot-pressed at 350 °C.

These results indicate that the milling with the YSZ vessel and balls improved the dimensionless figure of merit by suppressing the contamination with materials acting as carrier dopants. The improvements in thermoelectric properties were largely affected by the milling vessel and ball materials.

Acknowledgements

This study was supported by the Japan Society for the Promotion of Science (JSPS) KAKENHI Grant Number JP17K06863. We thank Helen McPherson, Ph.D., from Edanz Group (www.edanzediting.com/ac) for the editing of a draft of this manuscript.

References

[1] D.M. Rowe, General Principles and Theoretical Consideration, in: D.M. Rowe (Ed.), Thermoelectr. Handb. Macro to Nano, CRC Press, Taylor & Francis Group, Boca Raton, Londo, New York, 2006: cp. 1.

[2] T. Mori, S. Priya, G. Editors, Materials for energy harvesting : At the forefront of a new wave, MRS Bull. 43 (2019) 176–180. https://doi:10.1557/mrs.2018.32.

[3] I. Petsagkourakis, K. Tybrandt, X. Crispin, I. Ohkubo, T. Mori, Thermoelectric materials and applications for energy harvesting power generation, Sci. Technol. Adv. Mater. 19 (2018) 836–862. https://doi:10.1080/14686996.2018.1530938.

[4] G. Rogl, P. Rogl, Skutterudites, a most promising group of thermoelectric materials, Curr. Opin. Green Sustain. Chem. 4 (2017) 50–57. https://doi:10.1016/j.cogsc.2017.02.006.

[5] X. Zhao, X. Li, L. Chen, Y. Pei, S. Bai, X. Shi, T. Goto, Effect of Ge Doping on Thermoelectric Properties of $Sr_yCo_4Sb_{12-x}Ge_x$, Jpn. J. Appl. Phys. 47 (2008) 7470–7473. https://doi:10.1143/jjap.47.7470.

[6] X. Tang, Q. Zhang, L. Chen, T. Goto, T. Hirai, Synthesis and thermoelectric properties of *p*-type- and *n*-type-filled skutterudite $R_yM_xCo_{4-x}Sb_{12}$(*R*:Ce,Ba,Y;*M*:Fe,Ni), J. Appl. Phys. 97 (2005) 093712. https://doi:10.1063/1.1888048.

[7] X. Tang, H. Li, Q. Zhang, M. Niino, T. Goto, Synthesis and thermoelectric properties of double-atom-filled skutterudite compounds $Ca_mCe_nFe_xCo_{4-x}Sb_{12}$, J. Appl. Phys. 100 (2006). https://doi:10.1063/1.2375017.

[8] V. Nirmal Kumar, Y. Hayakawa, H. Udono, Y. Inatomi, Enhanced thermoelectric properties of InSb: Studies on In/Ga doped GaSb/InSb crystals, Intermetallics. 105 (2019) 21–28. https://doi:10.1016/j.intermet.2018.11.006.

[9] A. Tavassoli, A. Grytsiv, F. Failamani, G. Rogl, S. Puchegger, H. Müller, P. Broz, F. Zelenka, D. Macciò, A. Saccone, G. Giester, E. Bauer, M. Zehetbauer, P. Rogl, Intermetallics Constitution of the binary M-Sb systems (M = Ti , Zr , Hf) and physical properties of MSb_2, Intermetallics. 94 (2018) 119–132. https://doi:10.1016/j.intermet.2017.12.014.

[10] C. Okamura, T. Ueda, K. Hasezaki, Preparation of single-phase ZnSb thermoelectric materials using a mechanical grinding process, Mater. Trans. 51 (2010) 860–862. https://doi:10.2320/matertrans.MH200902.

[11] C. Okamura, T. Ueda, Kazuhiro Hasezaki, Preparation of Single Phase β-Zn_4Sb_3 Thermoelectric Materials by Mechanical Grinding Process, Mater. Trans. 51 (2010) 152–155. https://doi:10.2320/matertrans.M2009199.

[12] J. Duan, C. Zhu, M. Guan, P. Lu, Y. He, Z. Fu, L. Zhang, F. Xu, X. Shi, L. Chen, Multiple phase transitions and structural oscillations in thermoelectric Cu_2S at elevating temperatures, Ceram. Int. 44 (2018) 13076–13081. https://doi:10.1016/j.ceramint.2018.04.127.

[13] C. Zhu, Y. He, P. Lu, Z. Fu, F. Xu, H. Yao, L. Zhang, X. Shi, L. Chen, Multiple nanostructures in high performance $Cu_2S_{0.5}Te_{0.5}$ thermoelectric materials, Ceram. Int. 43 (2017) 7866–7869. https://doi:10.1016/j.ceramint.2017.03.103.

[14] J. Yu, K. Zhao, P. Qiu, X. Shi, L. Chen, Thermoelectric properties of

copper-deficient $Cu_{2-x}Se$ ($0.05 \leq x \leq 0.25$) binary compounds, Ceram. Int. 43 (2017) 11142–11148. https://doi:10.1016/j.ceramint.2017.05.161.

[15] M. Stordeur, Valence Band Structure and Thermoelectric Figure-of-Merit of $(Bi_{1-x}Sb_x)_2Te_3$ Crystals, in: D. M. Rowe (Ed.), CRC Handb. Thermoelectr., CRC Press, Taylor & Francis Group, Berlin Heidelberg, 1995: pp. 239–244.

[16] C. Kittel, Introduction to Solid State Physics, in: Second, John Wiley & Son, Inc, New York, 1953: p. 241.

[17] O. Meroz, Y. Gelbstein, Thermoelectric $Bi_2Te_{3-x}Se_x$ alloys for efficient thermal to electrical energy conversion, Phys. Chem. Chem. Phys. 20 (2018) 4092–4099. https://doi:10.1039/C7CP06176E.

[18] O. Meroz, D. Ben-Ayoun, O. Beeri, Y. Gelbstein, Development of $Bi_2Te_{2.4}Se_{0.6}$ alloy for thermoelectric power generation applications, J. Alloys Compd. 679 (2016) 196–201. https://doi:10.1016/j.jallcom.2016.04.072.

[19] H. Scherrer, S. Scherrer, Thermoelectric properties of bismuth antimony telluride solid solution, in: D. M. Rowe (Ed.), Thermoelectr. Handb. Macro to Nano, CRC Press, Taylor & Francis Group, Boca Raton, Londo, New York, 2006: p. ch. 27.

[20] F.H. Lin, C.J. Liu, A simple energy-saving aqueous synthesis of Bi_2Te_3 nanocomposites yielding relatively high thermoelectric power factors, Ceram. Int. 45 (2019) 9397–9400. https://doi:10.1016/j.ceramint.2018.08.170.

[21] J. Zheng, S. Chen, K. Cai, J. Yin, S. Shen, Preparation and thermoelectric properties of $Bi_2Se_xTe_{3-x}$ bulk materials, Ceram. Int. 43 (2017) 5920–

5924. https://doi:10.1016/j.ceramint.2017.01.085.

[22] A. Bhaskar, H.C. Lai, Y.L. Liu, C.J. Liu, Anisotropy measurements of a cuboid of nanostructured hydrothermally-prepared $Bi_{0.45}Sb_{1.55}Te_3$, Ceram. Int. 43 (2017) 17142–17147. https://doi:10.1016/j.ceramint.2017.09.135.

[23] M.K. Keshavarz, D. Vasilevskiy, R.A. Masut, S. Turenne, *p*-Type Bismuth Telluride-Based Composite Thermoelectric Materials Produced by Mechanical Alloying and Hot Extrusion, J. Electron. Mater. 42 (2013) 1429–1435. https://doi:10.1007/s11664-012-2284-2.

[24] Z. Wang, T. Araki, T. Onda, Z. Chen, Effect of annealing on microstructure and thermoelectric properties of hot-extruded Bi–Sb-Te bulk materials, J. Mater. Sci. 53 (2018) 9117–9130. https://doi:10.1007/s10853-018-2211-x.

[25] T. Hamachiyo, M. Ashida, K. Hasezaki, H. Matsunoshita, M. Kai, Z. Horita, Thermoelectric Properties of Bi_2Te_3-Related Materials Finely Grained by Mechanical Alloying and High Pressure Torsion, Mater. Trans. 50 (2009) 1592–1595. https://doi:10.2320/matertrans.E-M2009807.

[26] Q. Lognoné, F. Gascoin, Reactivity, stability and thermoelectric properties of n-Bi_2Te_3 doped with different copper amounts, J. Alloys Compd. 610 (2014) 1–5. https://doi:10.1016/j.jallcom.2014.04.166.

[27] K. Hirota, M. Kitamura, K. Takagi, K. Hasezaki, Thermoelectric Behaviors of $Bi_{0.3}Sb_{1.7}Te_{3.0}$ with Excess or Deficiency of Tellurium Prepared by Mechanical Alloying Followed by Hot Pressing, Mater. Trans. 59 (2018) 1233–1238. https://doi:10.2320/matertrans.MF201704.

[28] T. Shalev, O. Meroz, O. Beeri, Y. Gelbstein, Investigation of the Effect of $MoSe_2$ on the Thermoelectric Properties of *n*-Type $Bi_2Te_{2.4}Se_{0.6}$, J.

Electron. Mater. 44 (2014) 1402–1407. https://doi:10.1007/s11664-014-3381-1.

[29] C. Chen, B. Zhang, D. Liu, Z. Ge, Thermoelectric properties of $Cu_yBi_xSb_{2-x-y}Te_3$ alloys fabricated by mechanical alloying and spark plasma sintering, Intermetallics. 25 (2012) 131–135. https://doi:10.1016/j.intermet.2012.02.018.

[30] A. Pakdel, Q. Guo, V. Nicolosi, T. Mori, Enhanced thermoelectric performance of Bi-Sb–Te/Sb_2O_3 nanocomposites by energy filtering effect, J. Mater. Chem. A. 6 (2018) 21341–21349. https://doi:10.1039/c8ta08238c.

[31] Q. Lognoné, F. Gascoin, On the effect of carbon nanotubes on the thermoelectric properties of n-$Bi_2Te_{2.4}Se_{0.6}$ made by mechanical alloying, J. Alloys Compd. 635 (2015) 107–111. https://doi:10.1016/j.jallcom.2015.02.055.

[32] M.K. Keshavarz, D. Vasilevskiy, R.A. Masut, S. Turenne, Mechanical properties of bismuth telluride based alloys with embedded MoS_2 nano-particles, Mater. Des. 103 (2016) 114–121. https://doi:10.1016/j.matdes.2016.04.042.

[33] B. Poudel, Q. Hao, Y. Ma, Y. Lan, A. Minnich, B. Yu, X. Yan, D. Wang, A. Muto, D. Vashaee, X. Chen, J. Liu, M.S. Dresselhaus, G. Chen, Z. Ren, High-Thermoelectric Performance of Nanostructured Bismuth Antimony Telluride Bulk Alloys, Science (80-.). 320 (2008) 634–638. https://doi:10.1126/science.1156446.

[34] S. Kumar, D. Chaudhary, P. Kumar Dhawan, R.R. Yadav, N. Khare, Bi_2Te_3-MWCNT nanocomposite: An efficient thermoelectric material,

Ceram. Int. 43 (2017) 14976–14982. https://doi:10.1016/j.ceramint.2017.08.017.

[35] K. Hasezaki, M. Nishimura, M. Umata, H. Tsukuda, M. Araoka, Mechanical Alloying of BiTe and BiSbTe Thermoelectric Materials, Mater. Trans. JIM. 35 (1994) 428–432. https://doi:10.2320/matertrans1989.35.428.

[36] K. Hirota, K. Takagi, K. Hanasaku, K.L. Hasezaki, H. Saito, S. Hata, K. Hasezaki, Carbon observation by electron energy-loss spectroscopy and thermoelectric properties of graphite added bismuth antimony telluride prepared by mechanical alloying-hot pressing, Intermetallics. 109 (2019) 1–7. https://doi:10.1016/j.intermet.2019.03.005.

[37] B.A. Cook, J.L. Harringa, Solid-State Synthesis of Thermoelectric Materials, in: Thermoelectr. Handb. Macro to Nano, D. M. Rowe, Boca Raton, Londo, New York, 2006: ch.19.

[38] B. Madavali, H.S. Kim, K.H. Lee, Y. Isoda, F. Gascoin, S.J. Hong, Large scale production of high efficient and robust p-type Bi-Sb-Te based thermoelectric materials by powder metallurgy, Mater. Des. 112 (2016) 485–494. https://doi:10.1016/j.matdes.2016.09.089.

[39] C.C. Koch, J.D. Whittenberger, Mechanical milling / alloying of intermetallics, Intermetallics. 4 (1996) 339–355.

[40] S.A. Humphry-Baker, C.A. Schuh, Anomalous grain refinement trends during mechanical milling of Bi_2Te_3, Acta Mater. 75 (2014) 167–179. https://doi:10.1016/j.actamat.2014.04.032.

[41] M. Kitamura, K. Hirota, K. Hasezaki, Relationships between Thermoelectric Properties and Milling Rotational Speed on $Bi_{0.3}Sb_{1.7}Te_{3.0}$

Thermoelectric Materials, Mater. Trans. 59 (2018) 1225–1232. https://doi:10.2320/matertrans.MF201703.

[42] A. Sayyadi-Shahraki, S.M. Rafiaei, S. Ghadami, K.A. Nekouee, Densification and mechanical properties of spark plasma sintered Si_3N_4/ZrO_2 nano-composites, J. Alloys Compd. 776 (2019) 798–806. https://doi:10.1016/j.jallcom.2018.10.243.

[43] Masato Kitamura, Kazuhiro Hasezaki, Effect of Mechanical Alloying on Thermal Conductivity of Bi_2Te_3 -Sb_2Te_3, Mater. Trans. 57 (2016) 2153–2157. https://doi:10.2320/matertrans.M2016169.

[44] M. Orihashi, Y. Noda, K. Hasezaki, Surface Texture of Bi_2Te_3-Based Materials Deformed Under Pressure-Current Heating, in: Int. Conf. Thermoelectr., 2007: pp. 95–98.

[45] S. Turenne, T.H. Clin, D. Vasilevskiy, R.A. Masut, Finite Element Thermomechanical Modeling of Large Area Thermoelectric Generators based on Bismuth Telluride Alloys, J. Electron. Mater. 39 (2010) 1926–1933. https://doi:10.1007/s11664-009-1049-z.

[46] M. Fusa, N. Yamamoto, K. Hasezaki, Measurement of Seebeck coefficient and conductive behaviors of $Bi_2Te_{3-x}Se_x$ (x = 0.15-0.6) thermoelectric semiconductors without harmful dopants, Mater. Trans. 55 (2014) 942–946. https://doi:10.2320/matertrans.MB201301.

[47] N.D. Lowhorn, W. Wong-Ng, Z.Q. Lu, E. Tomas, M. Ohtani, M.L. Green, N.R. Dilley, J. Sharp, T.N. Tran, Development of a Seebeck coefficient Standard Reference Material, Appl. Phys. A Mater. Sci. Process. 96 (2009) 511–514. https://doi:10.1557/jmr.2011.118.

[48] K. Hasezaki, S. Wakazuki, T. Fujii, M. Kitamura, Constituent Element

Addition to *n*-Type $Bi_2Te_{2.67}Se_{0.33}$ ThermoelectricSemiconductor without Harmful Dopants by Mechanical Alloying, Mater. Trans. 57 (2016) 1001–1005. https://doi:10.2320/matertrans.M2016031.

[49] K. Uemura, I.A. Nishida, Thermoelectric Semiconductor and its Applications, in: Nikkankougyou Shinbunsha, Tokyo, 1988: pp. 195–197.

[50] T.M. Tritt, Thermal Conductivity Theory, Properties, and Applications, in: Plenum Publishers, New York, 2004: pp. 193–195.

[51] K.W. Schlichting, N.P. Padture, P.G. Klemens, Thermal conductivity of dense and porous yttria-stabilized zirconia, J. Mater. Sci. 36 (2001) 3003–3010. https://doi:10.1023/A:1017970924312.

[52] D. Benjamin, ed., Properties and Selection: Stainless Steel, Tool Materials and Special Purpose Metals, in: Met. Handb. , Vol.3, 9th ed., American Society for Metals, Ohio, 1980: pp. 34–35.

[53] Yoshio Suga, Thermoelectrics, in: Makisyoten, Tokyo, 1965: p. 317.

[54] R. Cohen, D.R. Lide, G.L. Trigg, eds., AIP Physics Desk Reference, in: 3rd ed., Springer-Verlag, New York, 2003: pp. 831–833.

Figure Captions

Fig. 1 XRD pattern of the milled $Bi_{0.3}Sb_{1.7}Te_{3.0}$ powder. The circles, squares, triangles, and solid circles represent Bi, Sb, and Te elements and $Bi_{0.3}Sb_{1.7}Te_{3.0}$ compound, respectively [29]. The standard peaks correspond to $Bi_{0.3}Sb_{1.7}Te_{3.0}$ (ICSD #184248).

Fig. 2 XRD patterns of the $Bi_{0.3}Sb_{1.7}Te_{3.0}$ disks sintered at 100–400 °C and milled at 150

rpm; main *hkl* indices of $Bi_{0.3}Sb_{1.7}Te_{3.0}$ are shown [29]. The standard peaks correspond to $Bi_{0.3}Sb_{1.7}Te_{3.0}$ (ICSD #184248).

Fig. 3 (a) SEM images and (b) Bi, (c) Sb, and (d) Te EDS-derived elemental distributions of the $Bi_{0.3}Sb_{1.7}Te_{3.0}$ disk sintered at 100 °C and milled at 150 rpm.

Fig. 4 SEM images of (a) a cross section and (b) fracture surface of the $Bi_{0.3}Sb_{1.7}Te_{3.0}$ disk sintered at 350 °C and milled at 150 rpm.

Fig. 5 (a) SEM image and (b) Bi, (c) Sb, (d) Te, (e) Zr, and (f) Y EDS-derived elemental distributions of the $Bi_{0.3}Sb_{1.7}Te_{3.0}$ disk sintered at 350 °C and milled at 150 rpm.

Fig. 6 Relationship between the electrical conductivity and sintering temperature for the $Bi_{0.3}Sb_{1.7}Te_{3.0}$ disks milled at 150 rpm at room temperature. The open circle corresponds to the $Bi_{0.3}Sb_{1.7}Te_{3.0}$ disk sintered at 350 °C and milled at 150 rpm with the stainless-steel vessel and Si_3N_4 balls [41].

Fig. 7 Relationship between the Seebeck coefficient and sintering temperature for the $Bi_{0.3}Sb_{1.7}Te_{3.0}$ disks milled at 150 rpm at room temperature. The open circle corresponds to the $Bi_{0.3}Sb_{1.7}Te_{3.0}$ disk sintered at 350 °C and milled at 150 rpm with the stainless-steel vessel and Si_3N_4 balls [41].

Fig. 8 Relationships between the total (solid circles), phonon (solid triangles), and carrier (solid squares) thermal conductivities and sintering temperature for the $Bi_{0.3}Sb_{1.7}Te_{3.0}$ disk milled at 150 rpm at room temperature. The open symbols correspond to the $Bi_{0.3}Sb_{1.7}Te_{3.0}$ disk sintered at 350 °C and milled at 150 rpm with the stainless-steel vessel and Si_3N_4 balls [41].

Fig. 9 Relationship between *ZT* and sintering temperature for the $Bi_{0.3}Sb_{1.7}Te_{3.0}$ disks milled at 150 rpm at room temperature. The open circle corresponds to the $Bi_{0.3}Sb_{1.7}Te_{3.0}$ disk sintered at 350 °C and milled at 150 rpm with the stainless-steel vessel and Si_3N_4 balls [41].

Fig. 10 XRD patterns of the disks sintered at 350 °C and milled at 110–180 rpm; main *hkl* indices of $Bi_{0.3}Sb_{1.7}Te_{3.0}$ are shown [29].

Fig. 11 Relationship between the electrical conductivity and milling speed for the $Bi_{0.3}Sb_{1.7}Te_{3.0}$ disks sintered at 350 °C with the YSZ milling vessel and balls at room temperature. The solid line corresponds to the $Bi_{0.3}Sb_{1.7}Te_{3.0}$ disks sintered at 350 °C and milled with the stainless-steel vessel and Si_3N_4 balls [41].

Fig. 12 Relationship between the Seebeck coefficient and milling speed for the $Bi_{0.3}Sb_{1.7}Te_{3.0}$ disks sintered at 350 °C and milled with the YSZ vessel and balls at room temperature. The solid line corresponds to the $Bi_{0.3}Sb_{1.7}Te_{3.0}$ disks sintered at 350 °C and milled with the stainless-steel vessel and Si_3N_4 balls [41].

Fig. 13 Relationships between the total, phonon, and carrier thermal conductivities and milling speed for the $Bi_{0.3}Sb_{1.7}Te_{3.0}$ disks sintered at 350 °C and milled with the YSZ vessel and balls at room temperature. The total, phonon, and carrier thermal conductivities are shown by the circles, triangles, and squares, respectively. The total, phonon, and carrier thermal conductivities of the $Bi_{0.3}Sb_{1.7}Te_{3.0}$ disk sintered at 350 °C and milled at 150 rpm with the stainless-steel vessel and Si_3N_4 balls are shown by the solid, dashed, and alternating-long–short dashed lines, respectively [41].

Fig. 14 Relationship between *ZT* and milling speed for the $Bi_{0.3}Sb_{1.7}Te_{3.0}$ disks sintered at 350 °C. The solid line corresponds to the $Bi_{0.3}Sb_{1.7}Te_{3.0}$ disks sintered at 350 °C and milled with the stainless-steel vessel and Si_3N_4 balls [41].

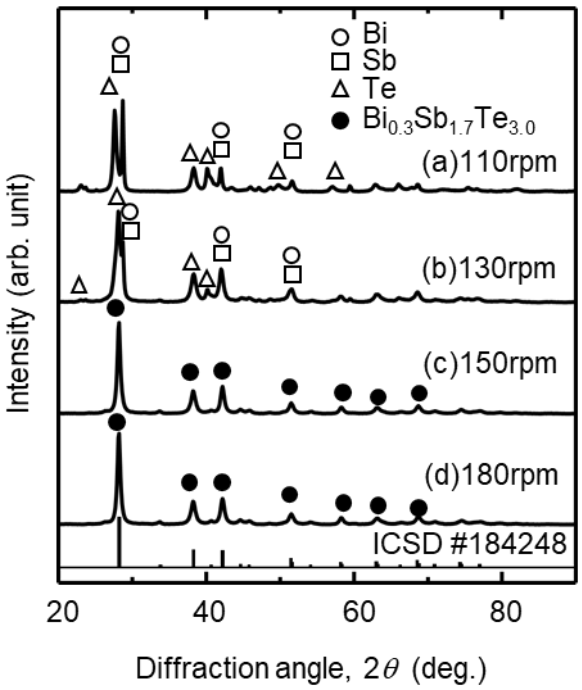

Fig. 1 XRD pattern of the milled $Bi_{0.3}Sb_{1.7}Te_{3.0}$ powder. The circles, squares, triangles, and solid circles represent Bi, Sb, and Te elements and $Bi_{0.3}Sb_{1.7}Te_{3.0}$ compound, respectively [29]. The standard peaks correspond to $Bi_{0.3}Sb_{1.7}Te_{3.0}$ (ICSD #184248).

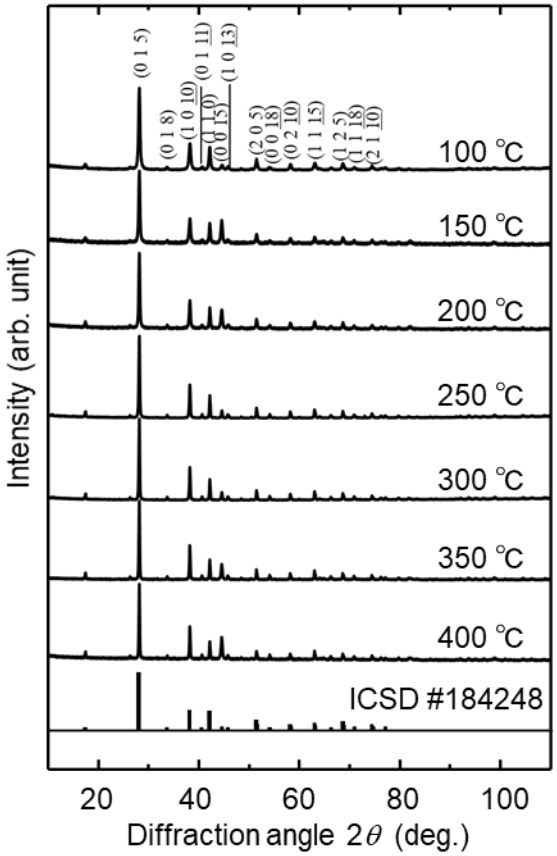

Fig. 2 XRD patterns of the $Bi_{0.3}Sb_{1.7}Te_{3.0}$ disks sintered at 100–400 °C and milled at 150 rpm; main *hkl* indices of $Bi_{0.3}Sb_{1.7}Te_{3.0}$ are shown [29]. The standard peaks correspond to $Bi_{0.3}Sb_{1.7}Te_{3.0}$ (ICSD #184248).

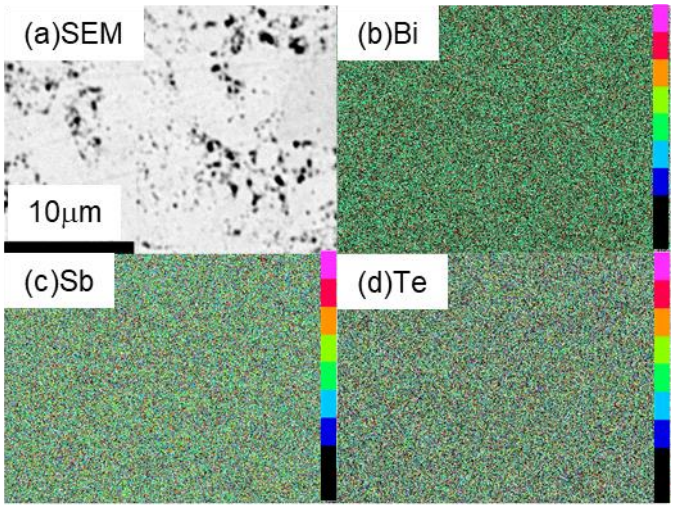

Fig. 3 (a) SEM images and (b) Bi, (c) Sb, and (d) Te EDS-derived elemental distributions of the $Bi_{0.3}Sb_{1.7}Te_{3.0}$ disk sintered at 100 °C and milled at 150 rpm.

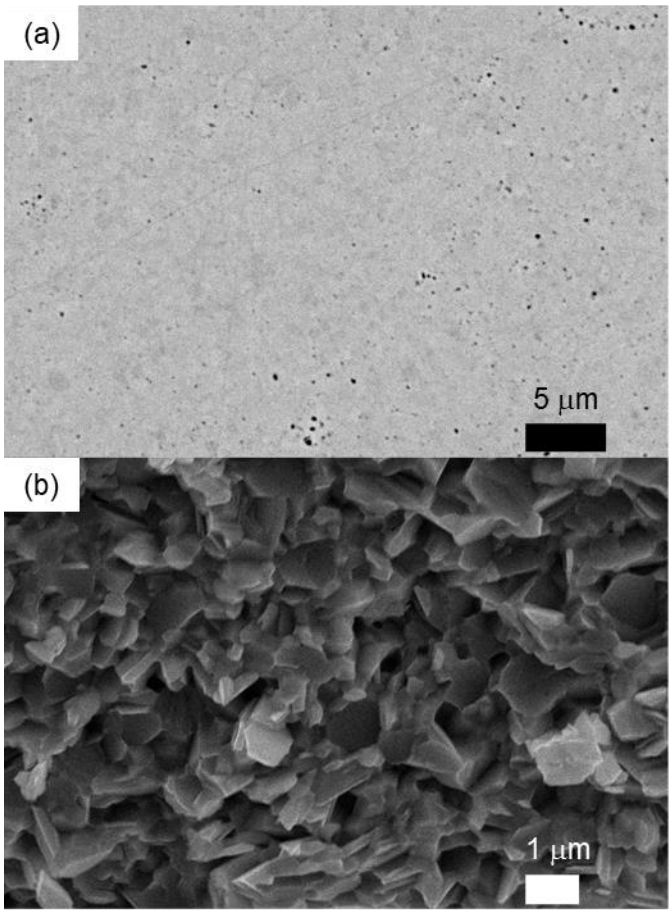

Fig. 4 SEM images of (a) a cross section and (b) fracture surface of the $Bi_{0.3}Sb_{1.7}Te_{3.0}$ disk sintered at 350 °C and milled at 150 rpm.

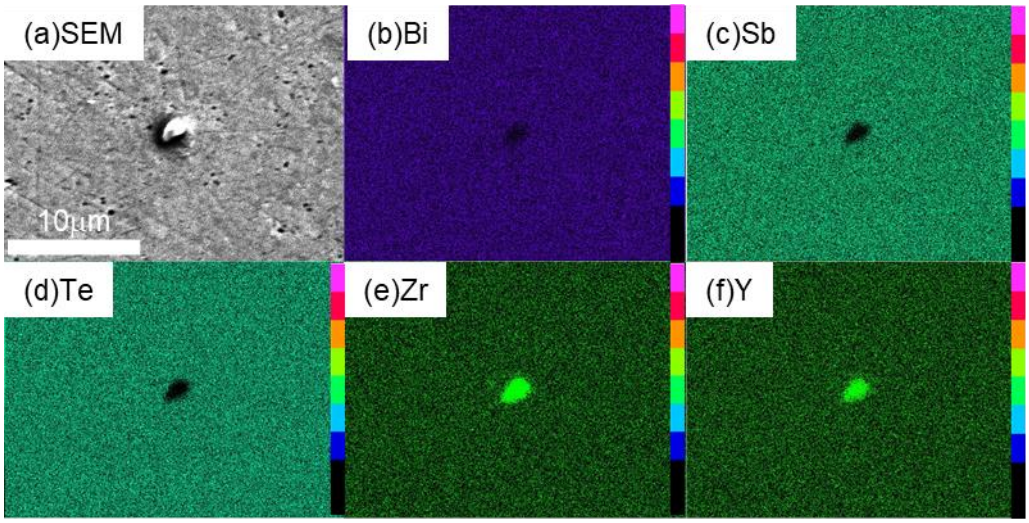

Fig. 5 (a) SEM image and (b) Bi, (c) Sb, (d) Te, (e) Zr, and (f) Y EDS-derived elemental distributions of the $Bi_{0.3}Sb_{1.7}Te_{3.0}$ disk sintered at 350 °C and milled at 150 rpm.

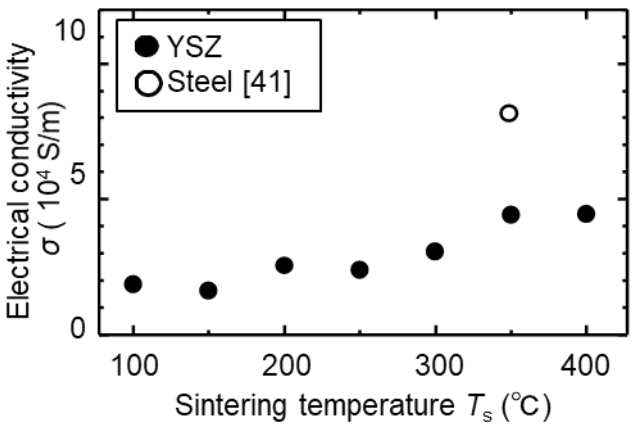

Fig. 6 Relationship between the electrical conductivity and sintering temperature for the $Bi_{0.3}Sb_{1.7}Te_{3.0}$ disks milled at 150 rpm at room temperature. The open circle corresponds to the $Bi_{0.3}Sb_{1.7}Te_{3.0}$ disk sintered at 350 ℃ and milled at 150 rpm with the stainless-steel vessel and Si_3N_4 balls [41].

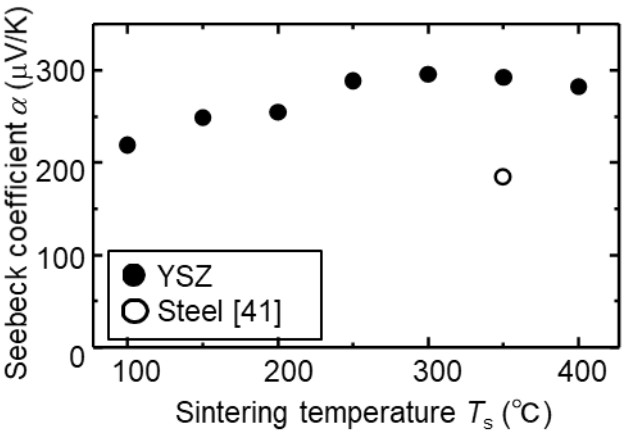

Fig. 7 Relationship between the Seebeck coefficient and sintering temperature for the $Bi_{0.3}Sb_{1.7}Te_{3.0}$ disks milled at 150 rpm at room temperature. The open circle corresponds to the $Bi_{0.3}Sb_{1.7}Te_{3.0}$ disk sintered at 350 ℃ and milled at 150 rpm with the stainless-steel vessel and Si_3N_4 balls [41].

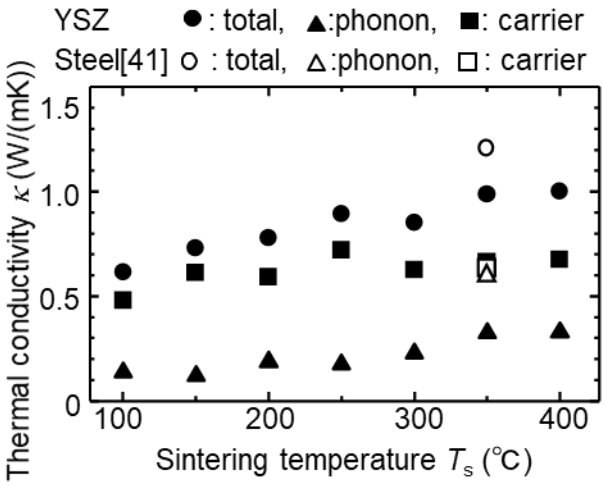

Fig. 8 Relationships between the total (solid circles), phonon (solid triangles), and carrier (solid squares) thermal conductivities and sintering temperature for the $Bi_{0.3}Sb_{1.7}Te_{3.0}$ disk milled at 150 rpm at room temperature. The open symbols correspond to the $Bi_{0.3}Sb_{1.7}Te_{3.0}$ disk sintered at 350 °C and milled at 150 rpm with the stainless-steel vessel and Si_3N_4 balls [41].

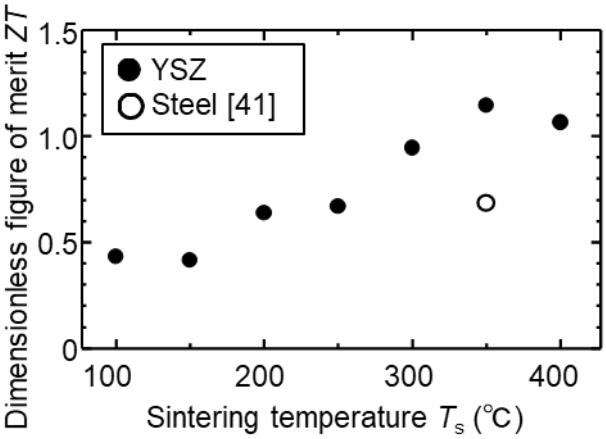

Fig. 9 Relationship between *ZT* and sintering temperature for the $Bi_{0.3}Sb_{1.7}Te_{3.0}$ disks milled at 150 rpm at room temperature. The open circle corresponds to the $Bi_{0.3}Sb_{1.7}Te_{3.0}$ disk sintered at 350 °C and milled at 150 rpm with the stainless-steel vessel and Si_3N_4 balls [41].

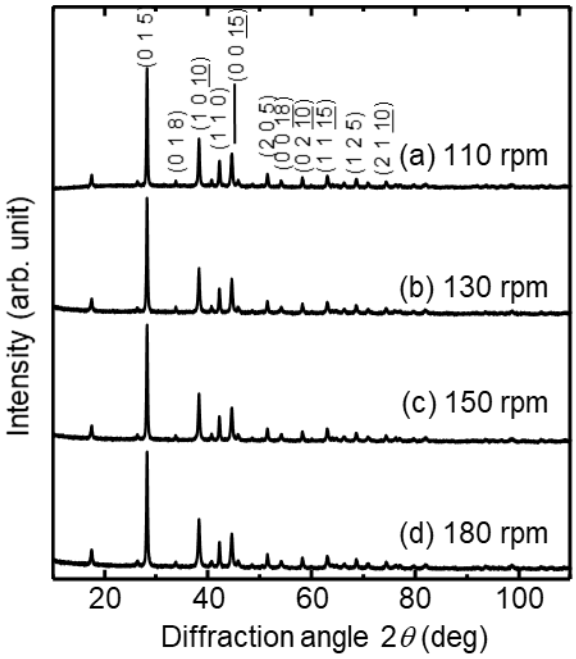

Fig. 10 XRD patterns of the disks sintered at 350 °C and milled at 110–180 rpm; main *hkl* indices of $Bi_{0.3}Sb_{1.7}Te_{3.0}$ are shown [29].

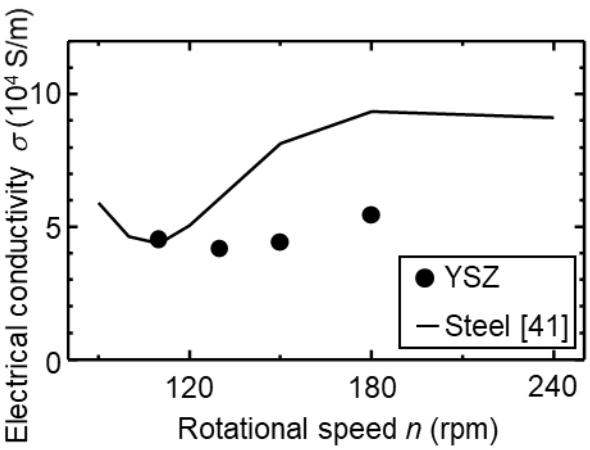

Fig. 11 Relationship between the electrical conductivity and milling speed for the $Bi_{0.3}Sb_{1.7}Te_{3.0}$ disks sintered at 350 °C with the YSZ milling vessel and balls at room temperature. The solid line corresponds to the $Bi_{0.3}Sb_{1.7}Te_{3.0}$ disks sintered at 350 °C and milled with the stainless-steel vessel and Si_3N_4 balls [41].